Flagella-like beating of actin bundles driven by self-organized myosin waves

Marie Pochitaloff, Martin Miranda, Mathieu Richard, Atitheb Chaiyasitdhi, Yasuharu Takagi, Wenxiang Cao, Enrique de la Cruz, James Sellers, J.-F. Joanny, Frank Jülicher, et al.

Flagella-like beating of actin bundles driven by self-organized myosin waves.

Marie Pochitaloff[1,†], Martin Miranda[2], Mathieu Richard[1], Atitheb Chaiyasitdhi[1], Yasuharu Takagi [3], Wenxiang Cao[4], Enrique M. De La Cruz[4], James R. Sellers[3], Jean-François Joanny[1,5], Frank Jülicher[2,6], Laurent Blanchoin[7,8], Pascal Martin[1*]

[1]*Laboratoire Physico-Chimie Curie, Institut Curie, Université PSL, Sorbonne Université, CNRS UMR168, F-75248 Paris, France.*

[2]*Max Planck Institute for the Physics of Complex Systems, 01187 Dresden, Germany.*

[3]*Laboratory of Molecular Physiology, National Heart, Lung and Blood Institute, NIH, Bethesda, MD 20892, USA*

[4]*Department of Molecular Biophysics and Biochemistry, Yale University, New Haven, CT 06520-8114, USA*

[5]*Collège de France, 11 place Marcelin Berthelot 75231 Paris Cedex 05, France*

[6]*Cluster of Excellence Physics of Life, Technische Universität Dresden, 01062 Dresden, Germany*

[7]*CytomorphoLab, Biosciences and Biotechnology Institute of Grenoble, Laboratoire de Physiologie Cellulaire & Végétale, Université Grenoble-Alpes/CEA/CNRS/INRA, 38054 Grenoble, France*

[8]*CytomorphoLab, Hôpital Saint Louis, Institut Universitaire d'Hématologie, UMRS1160, INSERM/AP-HP/Université Paris Diderot, 75010 Paris, France*

[†]*Present address: Department of Mechanical Engineering, UC Santa Barbara, 93106-5070 Santa Barbara, USA.*

[*]*To whom correspondence should be addressed: Email: pascal.martin@curie.fr*

ABSTRACT: Wave-like beating of eukaryotic cilia and flagella—threadlike protrusions found in many cells and microorganisms—is a classic example of spontaneous mechanical oscillations in biology. This type of self-organized active matter raises the question of the coordination mechanism between molecular motor activity and cytoskeletal filament bending. Here we show that in the presence of myosin motors, polymerizing actin filaments self-assemble into polar bundles which exhibit wave-like beating. Importantly, filament beating is associated with myosin density waves initiated at twice the frequency of the actin bending waves. A theoretical description based on curvature control of motor binding to the filaments and of motor activity explains our observations in a regime of high internal friction. Overall, our results indicate that the binding of myosin to actin depends on the actin-bundle shape, providing a feedback mechanism between myosin activity and filament deformations for the self-organization of large motor-filament assemblies.

Introduction

Biological systems can self-organize at large scales by orchestrating the local activity of many small constituents that each consume energy from the environment. The regular beating patterns exhibited by cilia and flagella provide a prototypical example of such self-organization. Using an in-vitro biomimetic approach, we study here minimal requirements for the emergence of spontaneous beating of polar bundles of bio-filaments driven by molecular motors.

Cilia and flagella of eukaryotes ranging from single cells to complex organisms share a complex common structure—the axoneme. The axoneme comprises a cylindrical arrangement of parallel filaments called microtubules, about 10,000 dynein motors uniformly distributed along the microtubules [1,2], as well as hundreds of other proteins [3]. Importantly, the flagellar beat—a regular oscillatory pattern of propagating bending waves—requires coordination of the motors both in time and along the length of the axoneme [2,4,5]. The dynamics of flagellar beating is a classical problem of theoretical biophysics. Many models have been developed to describe the feedback mechanisms specifying how the activity of the molecular motors depends on the filament-bundle shape [4–13]. However, the coupling between motor activity and flagellar beating is still a matter of debate [2]. In addition, although dissipation from external hydrodynamic drag on the flagellar outer surface is usually thought to balance power input from the motors, the contribution of internal sources of friction has recently been discussed [14–16].

Biomimetic in-vitro experiments with purified proteins [17–19] have demonstrated that spontaneous oscillations can emerge in motor ensembles under elastic loading, without the intervention of regulatory proteins or the external drive of an oscillatory biochemical signal. These experiments confirmed the predicted existence of generic oscillatory instabilities in motor systems [11,20,21]. In contrast to top-down approaches on functional cilia or flagella, in-vitro experiments afford an attractive means to control physical parameters such as the size of the system, geometrical constrains, or the properties of the motors at work, and thus to probe the physical underpinning of motor coordination in oscillatory systems.

In this work, we present a bottom-up approach based on a minimal active molecular system. We show that, in the presence of myosin motors, polymerizing actin filaments can self-assemble in vitro into polar bundles of filaments that spontaneously exhibit wave-like beating. The beating properties in this artificial system resemble those of eukaryotic flagella, despite the different molecular identity of the filaments and motors at work and despite the lack of regulatory proteins. We used surface micro-patterns of actin nucleators to control the geometry of actin-bundle formation in the presence of myosin motors. We analysed the properties of the emerging actin-bending waves as a function of the size of the actin bundle and of the identity

of the myosin motors that drive the oscillations. Importantly, we demonstrate that actin-bending waves are associated with myosin-density waves: myosin recruitment and localization on the actin bundle are dynamically coupled to the actin-bundle shape. A theoretical description based on curvature control of motor binding to the filaments and of motor activity explains our observations in a regime of high internal friction.

Results

We used surface micro-patterns—disks—of a nucleation-promoting factor to control the geometry and collective organization of actin polymerization [22–24]. Because of steric interactions, actin filaments grow perpendicular to the circular borders of the actin-nucleation zone by monomer addition to their barbed ends, resulting in radial polar networks of filaments (Supplementary Fig. 1). Previous work has demonstrated that the length of the actin filaments is exponentially distributed, with a mean length of about 8 μm [24]. Inclusion of a depleting agent ensured that most of the filaments grew parallel to the substrate and that the network remained within a few hundred nanometers of the passivated glass surface [25]; the depleting agent also facilitated bundle formation [26]. We performed the in-vitro polymerization assay in the presence of either heavy meromyosin II, which is a soluble two-headed fragment of skeletal muscle myosin II—hereafter called myosin II for simplicity, or of a two-headed fragment of myosin Va fused to the green-fluorescent protein—hereafter called myosin V. We found that growing actin filaments in the presence of myosin motors self-organized into bundles with a diameter that decreased from their proximal to their distal ends (Extended Data Fig. 1). Remarkably, the actin-filament bundles displayed periodic bending waves traveling from the base towards the tip of the bundle (Extended Data Fig. 1; Supplementary Videos 1-3). In the following, the index $'II'$ and $'V'$ refer to data obtained with myosin-II and myosin-V motors, respectively. Unless otherwise indicated, we provide averages and standard deviations (SD) of beating-bundle properties over ensembles of n bundles.

Actin-bending waves driven by myosin II. We analysed the beating properties of fluorescently-labelled actin bundles after 23 ± 8 min (mean ± SD; $n = 59$) of polymerization. At this time, the bundles had grown to a length $L_{II} = 15.9 \pm 6.1$ μm ($n = 59$). Automatic tracking of the center line of an actin-filament bundle (Fig. 1a; Supplementary Video 4) revealed beating patterns with a heart-shaped envelope in which the bundle's tip follows a characteristic 8-figure (Fig. 1b). These patterns resemble those reported for flagella of the bull sperm [27,28] but with slower beating kinetics. At any given arc length s, the angle $\psi(t, s)$ between the tangent to bundle's center line and the vertical axis (axis Y in Fig. 1c) displayed sinusoidal

oscillations as a function of time t (Fig. 1c-d) with a period $T_{II} = 15 \pm 9$ s ($n = 59$). The oscillation amplitude ψ_0 increased linearly from the base of the bundle to typically two-thirds of the total length at a rate $\psi_0' = 12.5 \pm 3.4$ deg/μm ($n = 59$), before saturating (Fig. 1d) and reaching a maximum value $\psi_{MAX} = 127 \pm 11$ deg ($n = 46$). Saturation was observed only when the bundle was long enough, typically $L_{II} > 11$ μm (Extended Data Fig. 2). The phase $\phi(s)$ of the tangent-angle oscillation decreased from the base ($s = 0$) to the tip ($s = L$) of the bundle, with a nearly linear relationship of slope ϕ' over most of the bundle's length (Fig. 1e). As a result, the wavelength $\lambda_{II} = -2\,\pi/\phi' = 17.1 \pm 5.8$ μm ($n = 59$) and the velocity $v_{II} = \lambda_{II}/T_{II} = 1.4 \pm 0.8$ μm/s (n = 59) of the corresponding traveling wave were nearly uniform along the bundle. A color plot of $\psi(t, s)$ recapitulates these observations; propagation of actin-bending waves at uniform velocities is visualized by linear iso-color lines (Fig. 1f). Wave propagation at uniform velocities is remarkable considering that the actin bundles are about one micrometer thick near their base, where they comprise hundreds of filaments, and get progressively thinner towards their tip, where they end with a single or only a few filaments. As discussed in Supplementary Information, bending-wave propagation at uniform velocity despite the structural heterogeneity of the filament bundle is most easily explained if an internal source of friction dominates external viscous drag on the bundle. Uniform wave velocities are also often observed in eukaryotic flagellar systems (e.g. [5]), but these flagella are based on a homogeneous axonemal structure comprising nine doublets of microtubules along most of the flagellar length.

The actin-filament bundles generally remained in focus within the observation plane of the spinning-disk microscope, indicating that the beating motion was almost planar. However, weak blinking of the actin-fluorescence intensity at a given arc length betrayed a small out-of-plane component to the beat that could result in oscillations of the projected bundle length (Extended Data Fig. 3, Supplementary Video 5). We analysed here the shape of the beat pattern within the plane of the beat.

Actin-bending waves driven by myosin V. To evaluate the generality of self-organized beating in polar bundles of actin filaments driven by myosin motors, we also performed experiments with myosin-V motors. Myosin II and myosin V are both double-headed molecular motors with movements directed toward the barbed ends of the actin filaments, thus away from the nucleation disks of actin polymerization. However, their biophysical properties and in-vivo functions differ strongly [29]: myosin II is a non-processive motor that normally works in large

groups to mediate muscle contraction, whereas myosin V is a processive motor that usually operates at the level of a single dimer or of a few dimers.

Despite these differences, we found that polar actin networks could also self-assemble into wave-like beating bundles under the action of myosin V (Fig. 2; Supplementary Videos 2 and 3). The heart-shaped beating patterns and 8-figures with myosin V were similar to those obtained with myosin II. Over an ensemble of $n = 29$ beating bundles of length $L_V = 18.3 \pm 5.4$ μm, actin-bending waves of wavelength $\lambda_V = 15.9 \pm 3.5$ μm travelled at nearly uniform velocities from bundle's base toward its tip, while the magnitude ψ_0 of tangent-angle oscillations grew along the length of the bundle at a rate $\psi_0' = 18.9 \pm 3.6$ deg/μm before reaching a maximum $\psi_{MAX} = 133 \pm 11$ deg. There is no statistical difference between the mean values of the bundle length and wavelength for myosin-II and myosin-V motors but the amplitude of tangent-angle oscillation increased more steeply with the arc length and the maximal tangent angle was slightly larger for myosin V (Table 1). The most striking difference between the two motor types was in the kinetics of the beating movements. Myosin V is known to be a slower motor than myosin II [30]. Accordingly, tangent-angle oscillations and the propagation of actin-bending waves were about 4-fold slower with myosin V (Fig. 2d; Table 1), corresponding to a period $T_V = 54 \pm 27$ s (n =29) and a travelling-wave velocity $v_V = 0.37 \pm 0.15$ μm/s (n = 29).

Effects of bundle length on beating properties. We observed self-organized beating for actin-filament bundles with a length L that ranged between 6 μm and 40 μm. Over this range, the wavelength λ of the bending waves displayed a positive correlation with the bundle length (Fig. 3a), both with myosin II (Pearson test: r = 0.72; p-value: $1.7\ 10^{-10}$) and with myosin V (Pearson test: r = 0.36; p-value: $1.1\ 10^{-3}$). Longer bundles showed longer wavelengths and the wavelength was on average nearly equal to the bundle length (Table 1). In ensemble averages, the oscillation period of the tangent angle displayed a weak positive correlation with the bundle length with myosin V (Pearson's test: $r = 0.36$; p-value = 0.05) but no significant correlation with myosin II (Pearson's test: $r = 0.2$; p-value = 0.13). However, because the beating actin bundles elongate at a velocity of 0.8 ±0.5 μm/min (n = 14) as polymerization proceeds, our in-vitro assay provides an attractive means to probe, in a single experiment, how the beating properties change with the bundle length while all other parameters remained fixed (Fig. 3b and c; Supplementary Video 6). With myosin II, beating was fast enough that the actin bundle length remained nearly constant over a few tens of oscillation cycles (Fig. 3b). In this case, we observed that the period of tangent-angle oscillation increased with the bundle's length at a

mean rate of 0.9 ± 0.7 s/μm (n = 5). In agreement with the observed increase of the wavelength with the bundle length (Fig. 3a), the travelling velocity of the actin-bending waves stayed nearly the same over the range of bundle length that we could explore (insert in Fig. 3c).

Interplay between actin-bending and myosin-density waves. Because myosin V was fused to the green-fluorescent protein (GFP), we could visualize the motors during wave-like beating of actin bundles (Supplementary Videos 7-9). In contrast to the monotonically decreasing and stationary actin-density profiles (Extended Data Fig. 4a), the myosin-density profiles exhibited a peak that appeared abruptly near the bundle's base and then travelled toward the bundle's tip, corresponding to a myosin-density wave (Fig. 4a). Thus, although they were added in bulk at a homogeneous concentration, the motors did not decorate the actin bundle according to the local actin density but were instead enriched within an apical region of the bundle. The myosin-fluorescence signal was elongated, conformed to the local shape of the bundle, and thus followed the bundle movement (Extended Data Fig. 5a). The myosin-density peak remained within a restricted region of the observation plane near the center of the 8-figure drawn by the bundle's tip (Extended Data Fig. 5b). As a result, when the beating bundle grew in length, the myosin-density peak moved together with the 8-figure (Supplementary Video 9; Extended Data Fig. 5c-d). Interestingly, plotting the ratio of myosin- and actin-density profiles revealed an increase of the motor density per actin filament during wave propagation (Extended Data Fig. 4b). The arc length at which the myosin density was maximal (Fig. 4d-e) displayed a sawtooth-shaped oscillation as a function of time. These observations suggest that myosin motors were periodically recruited in a proximal region of the filament bundle and released at the bundle's tip.

To describe how the myosin-density waves were coupled to the underlying actin-bending waves, we compared the myosin-density profiles (Fig. 4a and d) to the bundle-curvature profiles (Fig. 4b and c; Supplementary Video 10). By repeating these measurements over an ensemble of beating bundles, we observed that the myosin waves were produced at precisely twice the frequency of actin-bending waves, corresponding to periods of 20.7 ± 6.0 s and 41.1 ± 12.4 s ($n = 10$), respectively. The velocity $v_V^{myo} = 0.7 \pm 0.2$ μm/s ($n = 17$) of the myosin waves was 1.4 to 3 times the velocity reported for myosin-V transport in in-vitro gliding or bead assays [31–33] but comparable to that of in-vitro processive movements of single myosin-V molecules on actin filaments [34] and to transport velocities measured inside cells [35]. The myosin-density peak may travel towards the bundle's tip because the attached motors move processively along the actin filaments, or because motors continuously bind to the front and unbind from the rear of a travelling motor collection, or both. Because myosin recruitment did

not happen at the very base of the actin bundle but at a more apical position, the velocity of the myosin waves was on average only 1.7-fold larger than the velocity $v_V^{act} = 0.42 \pm 0.15$ μm/s (n = 17) of the corresponding actin bending waves.

Superimposing the myosin-density profiles (Fig. 4a) and the actin curvature profiles (Fig. 4b) provides the envelopes of the two interrelated waves. The amplitude of the actin-bundle curvature wave increased smoothly as the wave travelled from the bundle's base towards its tip before saturating. In contrast, the corresponding myosin density increased abruptly at a position $s^* = 6.9 \pm 1.8\ \mu m$ where the actin curvature reached a threshold value $C^* = 0.65 \pm 0.09\ \mu m^{-1}$, as measured over an ensemble of $n = 14$ beating bundles. This observation suggests that myosin recruitment from the bulk to the actin-filament bundle depends on the magnitude of the bundle's local curvature. At the time of recruitment, the myosin peak was localized near a position of maximal absolute curvature in the actin bundle (Fig. 4e, Extended Data Fig. 4; Supplementary Videos 7 and 10). At later times, while the waves continued traveling towards the bundle's tip, both the actin curvature and the myosin density remained at saturated values (Fig. 4a and b). However, because myosin waves travelled faster than actin-curvature waves, the myosin peak did not colocalize with the position of maximal absolute actin curvature but was positioned farther toward the bundle's tip (Fig. 4c-e, Extended Data Fig. 6). We note that the ratio of the standard deviation to the mean for the threshold curvature C^* was small, only 14%. Over the same ensemble of beating bundles, the bundle width $W^* = 0.66 \pm 0.09 \mu m$ $(n = 14)$ at the position s^* of myosin recruitment also showed small variations, indicating that the beating bundles were similar in our experiments.

Thus, visualization of the motors revealed a nonlinear self-organization process. Bending waves of the actin-filament bundles are associated with myosin-density waves generated at twice the frequency of bending oscillations. In the following, we present a theory showing how wave-like beating of an active filament bundle may emerge from a dynamic interplay between bending of the bundle and curvature-dependent motor binding to the filaments.

Physical description of self-organized beating. To account for our experimental observations, we built a coarse-grained theory of an active filament bundle that generates wave-like beating through a dynamic instability (Supplementary Information). The theory keeps track of a minimal set of mesoscopic variables as a function of time t and the arc length s: the angle $\psi(t, s)$ between the tangent to the center line of the bundle and the vertical axis, which describes the shape of the bundle, the total lineic density $\rho(t, s)$ of bound motors, and the algebraic lineic density $\rho_a(t, s)$ of active motor crosslinks that generate internal torques within the bundle. The

dynamic equations for these variables are obtained from symmetry arguments and conservation laws.

The active torques that drive beating are generated by motors that form transient crosslinks between filaments. A motor-mediated crosslink between a filament pair can produce a clockwise or an anticlockwise torque, depending on whether the motor advances on one or the other filament of the pair. We denote by $\rho_+(t,s)$ and $\rho_-(t,s)$ the corresponding lineic densities of active crosslinks in a cross-section of the filament bundle and we define the algebraic lineic density $\rho_a(t,s) = (\rho_+ - \rho_-)/N(s)$ of active crosslinks per filament. The bundle is a heterogeneous structure comprising aligned polar filaments of different lengths. The number $N(s)$ of filaments in a cross-section decreases exponentially with the arc length s. The net active torque at arc length s is given by $N(s)A_0\rho_a(t,s)$, where A_0 is the magnitude of the torque produced by an active crosslink. Here we propose that the active torque per filament and per unit length increases at a rate $A_0 k_a C$ proportional to bundle curvature $C = \partial_s \psi$ and relaxes at a rate k_d. A linear relation is expected if the radius of curvature of the bundle is larger than the diameter of the bundle's cross-section. The parameter k_a characterizes the curvature dependence of the active torque. This coupling generates a positive feedback between torque and curvature. Because of the delay due to binding and unbinding kinetics of active crosslinks, the active filament bundle can undergo an oscillatory instability—a Hopf bifurcation—beyond a critical value Ω_c of the control parameter $\Omega = A_0\, k_a/k_d$, resulting in the emergence of wave-like beating.

Beating of the filament bundle is associated with a density wave of bound motors $\rho(t,s)$, with abrupt motor recruitment beyond a threshold value of bundle curvature $C = C^*$. Because recruitment happens near the base of the filament bundle and is followed by propagation of a motor-density peak of constant amplitude, we propose that $C^* = C_0/N\,(s)$ is inversely related to the local number of filaments: the larger the local number of filaments, the easier it is to recruit motors upon bundle bending at this position. The mechanosensitivity of motor binding is thus a cooperative behavior of the filament bundle. Finally, we consider the simple limit in which dissipation is dominated by internal shear friction, with a friction coefficient per filament ξ_0, and that viscous drag by the surrounding fluid only provides a small contribution (see Section 6 in the Supplementary Information). This limit is valid for sufficiently short bundles. In this regime of high internal friction, the dynamic equation for $\psi(t,s)$ depends only weakly on the number of filaments in the bundle.

At the Hopf bifurcation ($\Omega = \Omega_c$), wave-like beating emerges at a frequency $\omega_c \simeq k_d\sqrt{\frac{2\pi^2}{L^2}\frac{\kappa_0}{\xi_0 k_d} + 1}$, in which L is the bundle length and κ_0 the bending rigidity per filament. For parameter values listed in Supplementary Tables S1 and S2, our numerical solutions show bending waves travelling from the base to the tip of the bundle at a nearly uniform velocity over most of the bundle's length and beating patterns with characteristic 8-figures (Fig. 5a-d). Curvature waves (Fig. 5e) are associated with motor-density waves (Fig. 5f; Supplementary Video 11). The motors bind to the filaments near the base of the bundle at twice the frequency of the bending oscillations. Motor binding corresponds to the sudden appearance of a localized motor-density peak $\rho(t, s)$ where and when the bundle reaches a threshold curvature (Fig. 5g). The motor-density wave then travels with a nearly constant magnitude towards the bundle's tip, with a velocity larger than that of the curvature wave (Fig. 5h). As in experiments, the myosin-density peak remained within a restricted region of the XY plane, near the center of the 8-figure in the beat pattern (Extended Data Figs. 5b and 7).

Overall, a simple model based on nonlinear curvature control of motor binding, on curvature control of active-torque generation, and on high internal shear friction captures the key features of the complex interplay between actin bending waves and myosin-density waves observed in experiments.

Discussion

Using a bottom-up approach based on a minimal active molecular system, we have demonstrated here that wave-like beating emerges robustly in polar bundles of actin filaments and myosin motors. In the presence of myosin-motor dimers added in bulk, growing actin filaments self-organize into beating bundles. Beating takes the form of bending waves with shapes resembling those observed in eukaryotic cilia and flagella, as well as in reconstituted kinesin-microtubule systems [19], despite the different families of filaments and motors at work. Thus, our finding provides further evidence that the emergence of wave-like oscillations is a generic feature of motor-filament systems, irrespective of the molecular details, providing experimental support for general theories of this form of active matter [11,21].

Our assay is based on protein micropatterning, which allows to control the self-assembly of actin-filament bundles and their spatial organization. In addition, visualization of the motors while the actin bundle is beating revealed that actin-bending waves are associated with myosin-density waves: the motor density increased abruptly beyond a threshold value of the bundle curvature before travelling towards the tip of the actin bundle (Fig. 4). These observations suggest that the filament-bundle shape regulates myosin *attachment* to actin, which could provide a feedback mechanism between motor activity and filament bending [8,9]. This mechanism contrasts with shape-dependent *detachment* as the basis of a dynamic instability that can give rise to spontaneous oscillations [5,36,37], although the two mechanisms are not mutually exclusive.

How could the motors' affinity for the filaments depend on the filament-bundle shape? There is a growing bulk of evidence showing that actin filaments are endowed with conformational plasticity [38–40] and that protein binding can stabilize a specific conformational state of actin as shown for myosin-V [41], in direct relevance to our work, as well as for other proteins [42,43]. Strong binding of myosin II has also been shown to reduce the helical angle of F-actin, elongating the filament [44]. Actin filaments therefore can act as mechanosensors because an applied force that alters their conformation should also affect their affinity for actin-binding proteins [40,45–48]. Myosin motor molecules are actin-binding proteins that can actively exert a physical stress on the filaments by converting energy from a biochemical fuel (here ATP) into mechanical work. Tension of only a few piconewtons—a magnitude comparable to that exerted by a single myosin motor [30]—appears to be strong enough to distort the actin-filament structure [49]. Thus, the actin filament does not operate simply as a passive cable to which proteins can bind but can provide feedback on protein binding and activity.

We have shown on general theoretical grounds that a positive feedback between curvature and active torque generation by the motors is sufficient for the emergence of self-organized bending waves in a polar-filament bundle (Fig. 5; Supplementary Information). This feedback mechanism is the simplest allowed by symmetry to linear order. Introducing nonlinearities that account for the observed curvature dependence of myosin binding, the theory reproduces quantitatively the main features of the experimental curvature and motor-density waves (Figs. 4 and 5, Supplementary Videos 7, 8, and 11). Curvature control of motor activity had earlier been proposed to mediate motor coordination in eukaryotic flagella [8,9], in particular to account for waveforms in isolated *Chlamydomonas* axonemes [12,16]. In our work, curvature control is described as an emergent behavior at a coarse-grained level based on symmetry arguments. As in studies of the flagellar beat that also invoke such feedback, we do not address here the detailed molecular mechanism by which the motors sense curvature of the filament bundle. This question remains a key open challenge in all these systems in view of the small estimated strains resulting from curvature changes in the filaments [12]. In addition, we cannot preclude that regulation of motor activity in our assay also involves other phenomena. In particular in the case of eukaryotic flagella a regulation by shear forces resulting from the interfilament sliding [4,5,11] or by transverse forces from variations of the interfilament lateral distance—a mechanism known as 'geometric clutch' [2] have been invoked. Such concepts could also be relevant to motor regulation in the assay studied here. Finally, future experiments ought to characterize the nature of individual motor motion within the myosin-density waves, test how curvature control of myosin binding depends on the number of filaments in the bundle, and determine quantitatively the relative importance of internal and external contributions to friction as a function of the architecture of the bundle.

In conclusion, our in-vitro work with a minimal acto-myosin system shows that the emergence of self-organized bending waves is a generic feature of motor-filament systems. We shed light on the dynamic interplay between myosin binding, myosin activity and the filament-bundle shape, opening an avenue for understanding the self-organization of this type of active matter.

Acknowledgements:

We are indebted to M. Rief for providing the heavy meromyosin II molecules. We thank the Cell and Tissue Imaging core facility (PICT-IBiSA) of the Institut Curie, a member of the French National Research Infrastructure France-BioImaging (ANR10-INBS-04). We thank John Manzi for protein purification and characterization, Fahima Di Federico for the genetic construct of His-pWA-Streptavidin, Jean-Yves Tinevez, Antoine Allard, and Isabelle Bonnet for help with Matlab programing, Hajer Ennomani and Christophe Guérin for help with actin micropatterning, and Julie Plastino and Cécile Sykes for fruitful discussions. This work was supported by the French National Agency for Research (ANR-12-BSV5 0014; awarded jointly to P.M. and L.B.), by the Labex Cell(n)Scale ANR-11-LABX-0038 and aNR-10-IDEX-001-02, by the United States National Institutes of Health Grant R35-GM135656 (awarded to E. M. D. L. C.), and by the European Research Council (741773 (AAA); awarded to L.B.).

Author Contributions Statement

M.P. and M.M. contributed equally to the work. M.P., M.M., M.R., A.C., J.F.J., F.J, L.B. and P.M. designed research, performed research, and analyzed data. Y.T., W.C., E.D.L.C, and J.S. provided new reagents. M.P., M.M., J.F.J, F.J., L.B, and P.M. wrote the manuscript.

Competing Interests Statement

The authors declare no competing interests.

Parameter	Definition	Myosin II (n = 59)	Myosin V (n = 29)	Statistical t-test
L (μm)	Bundle length	15.9 ± 6.1	18.3 ± 5.4	n.s.
λ (μm)	Wavelength of bending waves	17.1 ± 5.8	15.9 ± 3.5	n.s.
λ/L	Wavelength-Length ratio	1.1 ± 0.3	0.9 ± 0.3	**
ψ_0' (deg/μm)	Growth rate of tangent-angle oscillation	12.5±3.4	18.9±3.6	****
ψ_{MAX} (deg)	Maximal tangent angle	127±11	133±11	*
T (s)	Tangent-angle period	15±9	54±27	****
v (μm/s)	Bending-wave velocity	1.4±0.8	0.37±0.15	****

Table 1: Beating characteristics and statistical testing. The numerical values are given as mean ± standard deviation over an ensemble of n bundles. With myosin II, only 46 of the 59 bundles were long enough ($L > 11$ μm) to show saturation of the tangent angle; the value of ψ_{MAX} was thus determined with those ($n = 46$). To compare the mean values obtained with the two motor types, we used two-tailed unpaired Student's t-tests with Welch's correction. Stars correspond to p-values with *p < 0.05, **p < 0.01, ***p < 0.001, and ****p < 0.0001, whereas 'n.s.' (p > 0.05) indicates non-significant differences.

FIGURE LEGENDS

Fig. 1 | Beating of an actin-filament bundle with myosin II. **a,** Snapshots of the actin-filament bundle. Yellow box: The bundle (arrowhead) has grown to a length $L = 14.8$ μm from a micro-patterned, actin-nucleation disk. **b**, Beating pattern resulting from automatic tracking of the bundle's center line; same bundle as in **a**. The insert defines the tangent angle ψ at any point M of a bundle's center line; the arc length origin $s = 0$ is at the bundle's base (point O). **c,** Tangent angle $\psi(t, s)$ as a function of time t at the arc lengths $s = 5$ μm (purple) and $s = 10$ μm (magenta); the corresponding power-spectral densities are shown on the right and their peaks indicate an oscillation period $T = 11.2$ s. **d,** Amplitude $\psi_0(s) = \sqrt{2\langle(\psi(t,s) - \langle\psi(t,s)\rangle)^2\rangle}$ of the tangent-angle oscillation as a function of the arc length s. The growth rate in the linear portion of the curve is $\psi_0' = 16.2$ deg/μm. **e,** Phase ϕ of the Fourier amplitude at the beating frequency as a function of the arc length s. The slope to a linear fit to the relationship $\phi(s)$ provides the wavevector $q = 0.30$ rad/μm, corresponding to the wavelength $\lambda = 20.9$ μm and the propagation velocity $v = \lambda/T = 1.9$ μm/s of actin-bending waves. **f,** Color plot of the tangent angle $\psi(t, s)$ as a function of time t and arc length s.

Fig. 2 | Beating of an actin-filament bundle with myosin V. **a,** Beating pattern. **b**, Tangent-angle profile $\psi(s)$, defined as in Fig. 1b, at various times over one period of oscillation, with a 2-s time interval between successive profiles. **c**, Color plot of the tangent angle $\psi(t, s)$ as a function of time t and arc length s. The period of tangent-angle oscillation is here $T = 30.6s$ and the actin-filament bundle has an average visible length L =18 μm. **d**, Box plots (25^{th} and 75^{th} percentiles in cyan; median values in red; whiskers indicate maximal and minimal values) and data points for the period T of tangent-angle oscillations (top) and the velocity v of bending waves (bottom) driven by myosin II (black disks) and myosin V (white disks).

Fig. 3 | Beating properties as a function of actin-bundle length. **a**, Wavelength λ of actin-bending waves as a function of the actin-bundle length L for beating bundles driven by myosin II (black disks) or by myosin V (white disks). The dashed line is of slope unity. **b**, Color plots of the tangent angle ψ to an actin bundle's center line as a function of the arc length s and time. The four successive recordings were obtained with the same actin bundle. Each recording started at different times with respect to the initiation of actin polymerization, as indicated on top of each panel. Actin beating was here driven by myosin II and displayed stationary properties over the 1-min duration of each recording. **c**, Period T of tangent-angle oscillations and velocity v of actin bending waves (insert) as a function of the actin-bundle length L. The red line represents a linear fit of slope 0.33 ±0.12 s/μm (95%-confidence bounds) to the relationship $T(L)$. Error bars for L and T are standard deviations over the duration of each recording. Error bars for v are 95%-confidence bounds to linear fits of the relationship $\phi(s)$ between the phase of tangent-angle oscillations and the arc length. Same actin bundle as in **c**.

Fig. 4 | Interplay between myosin-V-density and actin-curvature waves. **a**, Myosin-density profiles (arbitrary units) during one period of a myosin-density wave, here 15.3 s. The order of the line colors, from dark blue to red, indicates time progression over one period of the myosin density waves with a 2-s time interval. **b,** Actin-curvature profiles during one period of bending oscillation, here 30.6 s. The actin-curvature profiles associated with the myosin-density profiles shown in **a** are shown using the same line colors. The grey areas in **a** and **b** were obtained by superimposing myosin-density and actin-curvature profiles, respectively, over 22 periods of bending oscillations, revealing the envelopes of the corresponding waves. **c**, Kymograph of actin-curvature profiles (arbitrary units). **d**, Kymograph of myosin-density profiles (arbitrary units). In **a-d**, there is a 2 s-interval between two successive profiles. **e**, Arc length as a function of time for the points along the bundle's center line at which the actin curvature is maximal (red disks), minimal (blue disks), and at which the myosin density peaks (black dots and line). For this bundle, the arc length $s^* = 8.3 \pm 0.9\mu m$ at which myosin density increases abruptly, corresponding to myosin recruitment in the actin bundle at a threshold curvature $C^* = 0.63 \pm 0.09\mu m^{-1}$, is marked by dashed lines in **a**, **b**, and **e**. The slope of the rising phase in saw-tooth oscillations of myosin density provided here a speed $v_V^{myo} = 0.7 \pm 0.2\mu\, m/s$ The standard deviations from the mean were here calculated over 29 periods of myosin density waves.

Fig. 5 | Wave-like beating in a model of an active filament bundle.

a, Wave-like beating pattern of the bundle's center line. **b**, Tangent angle $\psi(s,t)$ to the center lines shown in **a** as a function of the arc length s at successive values of time t over one period of bending oscillation. **c**, Curvature profiles $C(s,t) = \partial_s \psi$ resulting from the tangent-angle profiles $\psi(s,t)$ shown in **b**. **d**, Color plot of the tangent angle $\psi(s,t)$, revealing bending waves travelling from the base towards the tip of the bundle at a velocity of 0.56 μm/s and beating with a period of 30.6 s. The corresponding curvature waves $C(s,t)$ are associated with motor-density waves $\rho(s,t)$, both of which are shown as kymographs in **e** and **f**, respectively. **g**, Profiles $\rho(s,t)$ of the total density of bound motors. **h**, Arc length as a function of time of the points along the bundle's center line at which the bundle curvature is maximal (red line), minimal (blue line), and at which the motor density peaks (black solid line). The motor-density peak travels at a velocity of 1.1μm/s. There is a 2.2 s-interval between two successive profiles in **a-c** and **e-g**. The arc length $s = 7.2$ μm at which the motor density increases abruptly, corresponding to motor recruited in the actin bundle, is marked by a dashed line in **b**, **c,** and **f.** In **a-c** and **g,** the order of the line colors, from dark blue to red, indicates time progression over one period of the motor-density waves with a 2.2-s time interval. These results are numerical solutions of Equations S1-7 with parameter values listed in Table S2 (Supplementary Information).

References

1. Nicastro, D. The Molecular architecture of axonemes revealed by cryoelectron tomography. *Science* **313**, 944–948 (2006).
2. Lindemann, C. B. & Lesich, K. A. Flagellar and ciliary beating: the proven and the possible. *J. Cell Sci.* **123**, 519–528 (2010).
3. Pazour, G. J., Agrin, N., Leszyk, J. & Witman, G. B. Proteomic analysis of a eukaryotic cilium. *J. Cell Biol.* **170**, 103–113 (2005).
4. Brokaw, C. J. Molecular mechanism for oscillation in flagella and muscle. *Proc. Natl. Acad. Sci. USA* **72**, 3102–3106 (1975).
5. Riedel-Kruse, I. H., Hilfinger, A., Howard, J. & Julicher, F. How molecular motors shape the flagellar beat. *HFSP J* **1**, 192–208 (2007).
6. Machin, K. E. Wave propagation along flagella. *J. Exp. Biol.* **35**, 796–806 (1958).
7. Brokaw, C. J. Computer simulation of flagellar movement VIII: Coordination of dynein by local curvature control can generate helical bending waves. *Cell Motil. Cytoskeleton* **53**, 103–124 (2002).
8. Brokaw, C. & Rintala, D. Computer simulation of flagellar movement. III. Models incorporating cross-bridge kinetics. *J. Mechanochem. Cell* **3**, 77–86 (1975).
9. Hines, M. & Blum, J. J. Bend propagation in flagella. I. Derivation of equations of motion and their simulation. *Biophys. J.* **23**, 41–57 (1978).
10. Lindemann, C. B. A 'Geometric Clutch' Hypothesis to explain oscillations of the axoneme of Cilia and Flagella. *J. Theor. Biol.* **168**, 175–189 (1994).
11. Camalet, S. & Jülicher, F. Generic aspects of axonemal beating. *New J. Phys.* **2**, 24–24 (2000).
12. Sartori, P., Geyer, V. F., Scholich, A., Julicher, F. & Howard, J. Dynamic curvature regulation accounts for the symmetric and asymmetric beats of Chlamydomonas flagella. *Elife* **5**, e13258 (2016).

13. Oriola, D., Gadêlha, H. & Casademunt, J. Nonlinear amplitude dynamics in flagellar beating. *R. Soc. Open Sci.* **4**, 160698 (2017).
14. Mondal, D., Adhikari, R. & Sharma, P. Internal friction controls active ciliary oscillations near the instability threshold. *Sci. Adv.* **6**, eabb0503 (2020).
15. Nandagiri, A. *et al.* Flagellar energetics from high-resolution imaging of beating patterns in tethered mouse sperm. *eLife* **10**, e62524 (2021).
16. Geyer, V. F., Howard, J. & Sartori, P. Ciliary beating patterns map onto a low-dimensional behavioural space. *Nat. Phys.* **18**, 332–337 (2022).
17. Bourdieu, L. *et al.* Spiral defects in motility assays: A measure of motor protein force. *Phys. Rev. Lett.* **75**, 176–179 (1995).
18. Placais, P. Y., Balland, M., Guerin, T., Joanny, J. F. & Martin, P. Spontaneous oscillations of a minimal actomyosin system under elastic loading. *Phys. Rev. Lett.* **103**, 158102 (2009).
19. Sanchez, T., Welch, D., Nicastro, D. & Dogic, Z. Cilia-like beating of active microtubule bundles. *Science* **333**, 456–9 (2011).
20. Jülicher, F. & Prost, J. Spontaneous Oscillations of Collective Molecular Motors. *Phys. Rev. Lett.* **78**, 4510–4513 (1997).
21. Guerin, T., Prost, J., Martin, P. & Joanny, J. F. Coordination and collective properties of molecular motors: theory. *Curr. Opin. Cell Biol.* **22**, 14–20 (2010).
22. Reymann, A. C. *et al.* Nucleation geometry governs ordered actin networks structures. *Nat Mater* **9**, 827–32 (2010).
23. Reymann, A. C., Guerin, C., Thery, M., Blanchoin, L. & Boujemaa-Paterski, R. Geometrical control of actin assembly and contractility. *Methods Cell Biol.* **120**, 19–38 (2014).
24. Richard, M. *et al.* Active cargo positioning in antiparallel transport networks. *Proc Natl Acad Sci USA* **116**, 14835–14842 (2019).

25. Letort, G. *et al.* Geometrical and mechanical properties control actin filament organization. *PLoS Comput. Biol.* **11**, e1004245 (2015).
26. Köhler, S., Lieleg, O. & Bausch, A. R. Rheological characterization of the bundling transition in F-actin solutions induced by methylcellulose. *PLoS ONE* **3**, e2736 (2008).
27. Gray, J. The movement of the spermatozoa of the bull. *J. Exp. Biol.* **35**, 96–108 (1958).
28. Rikmenspoel, R. Movements and active moments of bull sperm flagella as a function of temperature and viscosity. *J. Exp. Biol.* **108**, 205 (1984).
29. De La Cruz, E. M. & Ostap, E. M. Relating biochemistry and function in the myosin superfamily. *Curr. Opin. Cell Biol.* **16**, 61–67 (2004).
30. Howard, J. *Mechanics of Motor Proteins and the Cytoskeleton*. (Sinauer Associates, 2001).
31. Mehta, A. D. *et al.* Myosin-V is a processive actin-based motor. *Nature* **400**, 590–593 (1999).
32. Rief, M. *et al.* Myosin-V stepping kinetics: A molecular model for processivity. *Proc. Natl. Acad. Sci. USA* **97**, 9482–9486 (2000).
33. Clemen, A. E. *et al.* Force-dependent stepping kinetics of myosin-V. *Biophys. J.* **88**, 4402–10 (2005).
34. Sakamoto, T. *et al.* Neck length and processivity of myosin V. *J. Biol. Chem.* **278**, 29201–7 (2003).
35. Pierobon, P. *et al.* Velocity, processivity, and individual steps of single myosin V molecules in live cells. *Biophys. J.* **96**, 4268–75 (2009).
36. Howard, J. Mechanical signaling in networks of motor and cytoskeletal proteins. *Annu. Rev. Biophys.* **38**, 217–34 (2009).
37. Ma, R., Klindt, G. S., Riedel-Kruse, I. H., Jülicher, F. & Friedrich, B. M. Active phase and amplitude fluctuations of flagellar beating. *Phys. Rev. Lett.* **113**, 048101 (2014).

530 38. Egelman, E. H., Francis, N. & DeRosier, D. J. F-actin is a helix with a random variable
531 twist. *Nature* **298**, 131–5 (1982).
532 39. Galkin, V. E., Orlova, A., Schroder, G. F. & Egelman, E. H. Structural polymorphism in F-
533 actin. *Nat. Struct. Mol. Biol.* **17**, 1318–23 (2010).
534 40. Galkin, V. E., Orlova, A. & Egelman, E. H. Actin filaments as tension sensors. *Curr. Biol.*
535 **22**, R96-101 (2012).
536 41. Kozuka, J., Yokota, H., Arai, Y., Ishii, Y. & Yanagida, T. Dynamic polymorphism of single
537 actin molecules in the actin filament. *Nat. Chem. Biol.* **2**, 83–6 (2006).
538 42. McGough, A., Pope, B., Chiu, W. & Weeds, A. Cofilin changes the twist of F-actin:
539 implications for actin filament dynamics and cellular function. *J. Cell. Biol.* **138**, 771–81
540 (1997).
541 43. Risca, V. I. *et al.* Actin filament curvature biases branching direction. *Proc. Natl. Acad. Sci*
542 *USA* **109**, 2913–8 (2012).
543 44. Tsaturyan, A. K. *et al.* Strong binding of myosin heads stretches and twists the actin helix.
544 *Biophys. J.* **88**, 1902–10 (2005).
545 45. Jegou, A. & Romet-Lemonne, G. The many implications of actin filament helicity. *Semin.*
546 *Cell Dev. Biol.* **102**, 65–72 (2020).
547 46. Mei, L. *et al.* Molecular mechanism for direct actin force-sensing by α-catenin. *eLife* **9**,
548 e62514 (2020).
549 47. Winkelman, J. D., Anderson, C. A., Suarez, C., Kovar, D. R. & Gardel, M. L. Evolutionarily
550 diverse LIM domain-containing proteins bind stressed actin filaments through a conserved
551 mechanism. *Proc. Natl. Acad. Sci. USA* 202004656 (2020).
552 48. Sun, X. *et al.* Mechanosensing through Direct Binding of Tensed F-Actin by LIM Domains.
553 *Dev. Cell* **55**, 468-482.e7 (2020).

554 49. Shimozawa, T. & Ishiwata, S. Mechanical distortion of single actin filaments induced by
555 external force: detection by fluorescence imaging. *Biophys. J.* **96**, 1036–44 (2009).
556

Methods

Micropatterning of an actin nucleation-promoting factor. The fusion protein His-pWA-Streptavidin (also called S-pVCA) was produced and characterized following a published protocol [50]; the histidine tag (His) was used for purification purposes and the streptavidin had no function in this work. The protein pWA comprises the C-terminal domain from the WASP/Scar proteins, a ubiquitous family of proteins that initiate actin polymerization on a pre-existing actin filament in the presence of the Arp2/3 complex and actin monomers. Micropatterning of this actin nucleation-promoting factor was performed as previously described [22–24]. In short, glass coverslips were oxidized for 2 min with an oxygen plasma and then passivated by incubating them with 0.1 mg/mL poly(L-lysine)-graft-poly(ethylene glycol) (PLL-g-PEG ; Jenkem Technology) in 10 mM 4-(2-hydroxyethyl)-1-piperazineethanesulfonic acid (HEPES) at pH 7.4 for 1 hour. The passivated surfaces were exposed to deep ultraviolet light (wavelength: 180 nm; UVO Cleaner Unit 342; Jelight Company Inc.) for 5 min through a transparent micropattern printed on a chromium synthetic quartz photomask (Toppan Photomasks). The coverslips were then incubated with 1 µM His-pWA-Streptavidin in a buffer containing 50 mM KCl, 1 mM MgCl2, 1 mM ethylene glycol-bis(β-aminoethyl ether)-N,N,N′,N′-tetraacetic acid) (EGTA), and 10 mM imidazole-HCl at a pH of 7.8 for 10 min. In our experiments, the pattern was typically composed of 9-µm diameter disks.

Actin polymerization in the presence of myosin motors. Actin polymerization from surface micro-patterns of the nucleation-promoting factor His-pWA-Streptavidin was induced in a solution containing 2 µM globular actin (Tebu-Bio), 8 µM profilin (produced as described in [50]), 80 nM Arp2/3 complex (Tebu-Bio), and myosin molecular motors. We used one of 2 types of myosin molecules. First, double-headed heavy meromyosin II—here simply called myosin II, purified from rabbit pectoral muscle according to a published protocol [51], was provided by the group of Matthias Rief (Technische Universität München, Munich, Germany) and used at a typical concentration of 500 nM (range: 250 nM-1500 nM). Second, recombinant double-headed myosin Va missing the C-terminal globular tail and fused to the green-fluorescent protein (GFP)—here called myosin V—was produced as described [52] and used at a concentration of 50 nM. The buffer of the acto-myosin polymerization solution was composed of 10 mM imidazole-HCl (pH 7.8), 50 mM KCl, 1 mM $MgCl_2$, 4.2 mM disodium adenosine triphosphate (ATP), 56 mM dithiothreitol (DTT), 0.1 mg/mL glucose, 42 nM catalase, 0.6 mM glucose oxidase, and 0.3% (w/v) methylcellulose. Using an Ubbelohde viscometer (type Ib; SI Analytics), we measured a viscosity of 15 mPa·s for this solution at 27°C. In order to visualize

actin filaments, 10% of the monomers were labeled with a fluorophore (Alexa568; Life Technologies). A thermostat-controlled chamber ensured that experiments were performed at a constant temperature of 27°C.

Microscopic Observations. Our samples were observed through a ×60 objective (numerical aperture:1.4) of a spinning-disk confocal microscope (Eclipse 80i; Nikon). Time-lapse videos were recorded with an EMCCD camera (Ultra897 iXon) at time intervals from 0.2 to 2 s. Time-lapse recordings could start as early as 5 min after the injection of the polymerization mix into the flow chamber and last up to 1 hour.

Image analysis. We used the ridge-detection plugin [53] of the image-processing software ImageJ (NIH) to automatically track the center line of actin-filament bundles. The bundles appeared as bright curvilinear objects on a dark background as a result of actin fluorescent labelling (Fig. 1a). Regions of interest with well-separated bundles were first selected. Only the beating part of the bundle was selected. A region of interest could encompass most of the bundle's length, from the border of the actin-nucleation area to the bundle's tip (Supplementary Video 1; yellow box in Extended Data Fig. 1d), or be positioned some distance away from the nucleation area (as in Supplementary Videos 3 and 8; yellow bow in Extended Data Fig 1f). If necessary, a rotation was applied on the selected regions to orient the base of the target bundle vertically. Neighboring bundles were deleted from the grayscale images to ensure that the tracking procedure did not yield parasite sets of coordinates. The output of the ridge-detection plugin was a stack of images, each showing the bundle's center line as a black line on a white background at a given time point. In each image, we then extracted and ordered the coordinates (X, Y) of the detected line. These coordinates were each smoothed using a moving average with a span of 5 points, before computing the arc length s along the bundle's centerline. After a linear interpolation of the relations $\big(X(s), Y(s)\big)$ with an arc-length increment of $0.01\mu m$, corresponding to about $1/25^{th}$ of the pixel size, we parametrized the shape of the center line by computing, at each point of the line, the tangent angle $\psi(t, s)$ relative to the vertical axis (Y-axis). At each time t, the relation $\psi(s)$ was then smoothed using a gaussian filter with a standard deviation of 100 points, corresponding to a distance of 1 μm or about $1/20^{th}$ of the wavelength of the bending waves, before computing the local curvature $\psi'(t, s) = d\psi/ds$. The base of the bundle was located at $s = 0$ and its tip at $s = L$, where the bundle's length$L(t)$ increased slowly over time as a result of actin polymerization. The amplitude of tangent-angle oscillations (Fig. 1d) was defined as $\psi_0(s) = \sqrt{2\langle(\psi(t,s) - \langle\psi(t,s)\rangle)^2\rangle}$, where $\langle\cdot\rangle$ denote a time average over the duration of the recording. Their period T and phase $\phi(s)$ was obtained from the

frequency $1/T$ and phase at the peak of the Fourier transform $\Phi(\omega, s) = \int \psi(t, s) e^{-i\omega t} dt$. We then calculated the local wavelength $\lambda(s) = -2\pi/\phi'$ and velocity $v = \lambda/T$ of the actin-bending waves. Myosin-density profiles $\rho(t, s)$ were obtained by computing, as a function of time, the intensity of the myosin-fluorescent signal along the actin bundle's center line. The speed of myosin-density wave was obtained by tracking the arc length of the myosin-density peak along the bundle as a function of time, as shown in Fig. 4e (black line). Data analysis was performed using custom software written in Matlab (the Mathworks).

Statistical testing. Unless otherwise indicated, all the results are quoted as mean ± standard deviation over an ensemble of n actin-filament bundles. Statistical significance of the difference between the means over two data ensembles, in practice data obtained with beating bundles driven with myosin II and myosin V, was assessed using a two-tailed Student's t-test with Welch correction. Correlations were assessed by computing a Pearson's correlation coefficient and its p-value.

Data availability statement

Source data are available for this paper. All other data that support the plots within this paper and other findings of this study are available from the corresponding author upon reasonable request.

References

50. Carvalho, K. *et al.* Actin polymerization or myosin contraction: two ways to build up cortical tension for symmetry breaking. *Philos. Trans. R. Soc. Lond. B Biol. Sci.* **368**, 20130005 (2013).

51. Margossian, S. S. & Lowey, S. Preparation of myosin and its subfragments from rabbit skeletal muscle. *Methods Enzym.* **85 Pt B**, 55–71 (1982).

52. Snyder, G. E., Sakamoto, T., Hammer, J. A., Sellers, J. R. & Selvin, P. R. Nanometer Localization of single green fluorescent proteins: evidence that myosin V walks hand-over-hand via telemark configuration. *Biophys. J.* **87**, 1776–1783 (2004).

53. Steger, C. An unbiased detector of curvilinear structures. *IEEE Trans. Pattern Anal. Mach. Intell.* **20**, 113–125 (1998).

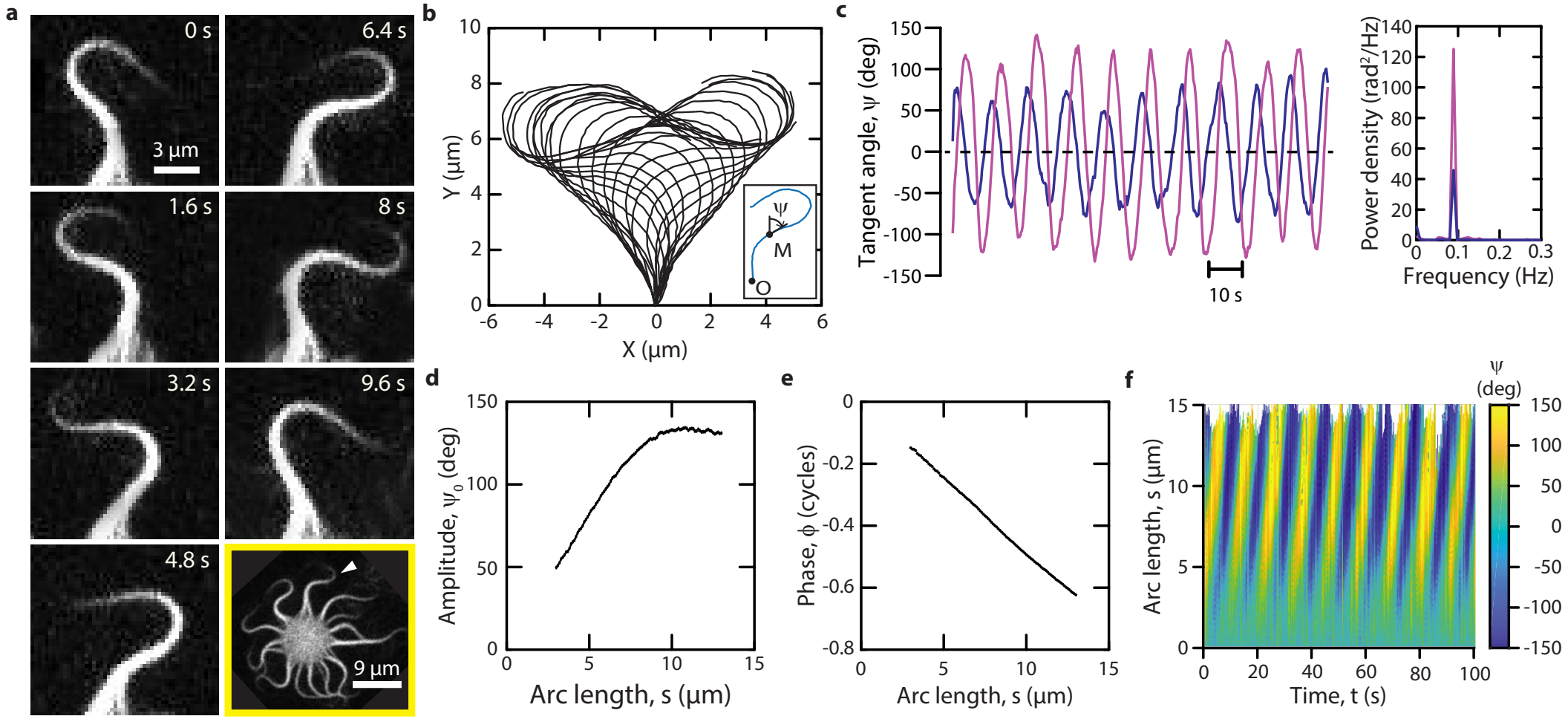
a
0 s
6.4 s
3 µm
1.6 s
8 s
3.2 s
9.6 s
4.8 s
9 µm
b
Y (µm)
X (µm)
ψ
M
O
c
Tangent angle, ψ (deg)
10 s
Power density (rad²/Hz)
Frequency (Hz)
d
Amplitude, ψ0 (deg)
Arc length, s (µm)
e
Phase, ϕ (cycles)
Arc length, s (µm)
f
ψ (deg)
Arc length, s (µm)
Time, t (s)

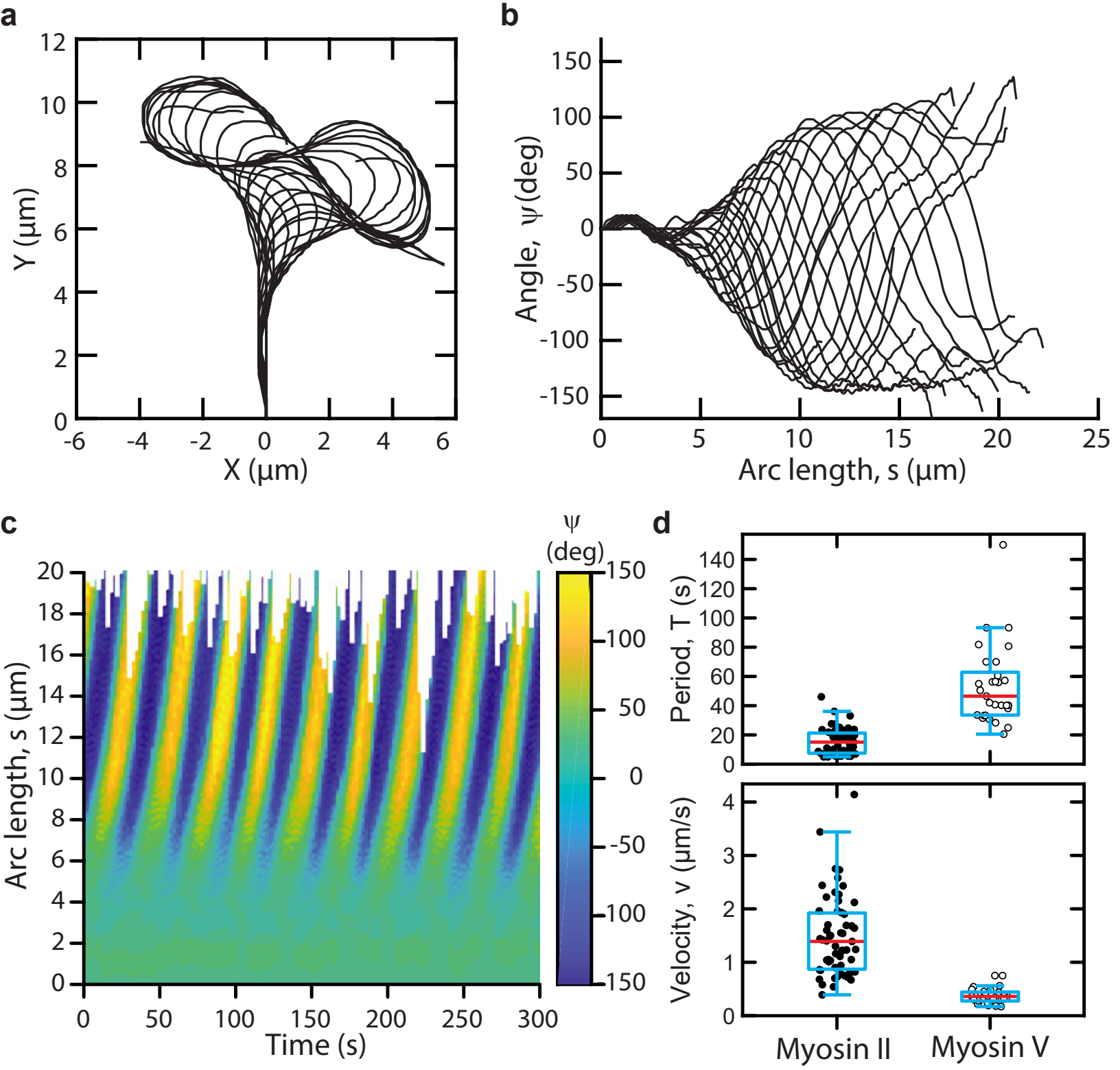
a
Y (μm)
X (μm)
b
Angle, ψ (deg)
Arc length, s (μm)
c
Arc length, s (μm)
Time (s)
ψ (deg)
d
Period, T (s)
Velocity, v (μm/s)
Myosin II
Myosin V

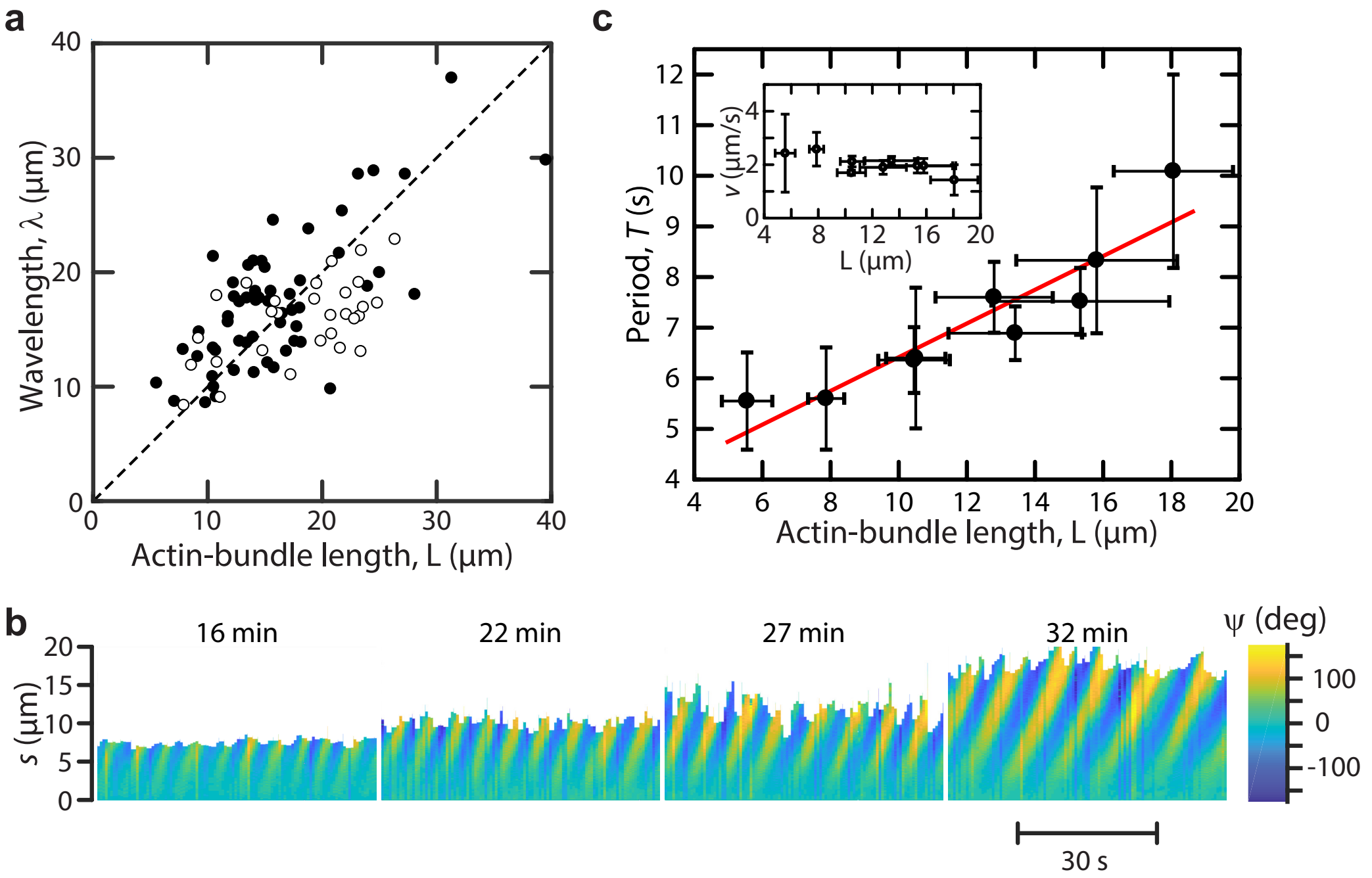
a
Wavelength, λ (μm)
Actin-bundle length, L (μm)
0
10
20
30
40
c
Period, T (s)
Actin-bundle length, L (μm)
v (μm/s)
L (μm)
b
16 min
22 min
27 min
32 min
s (μm)
ψ (deg)
100
0
-100
30 s

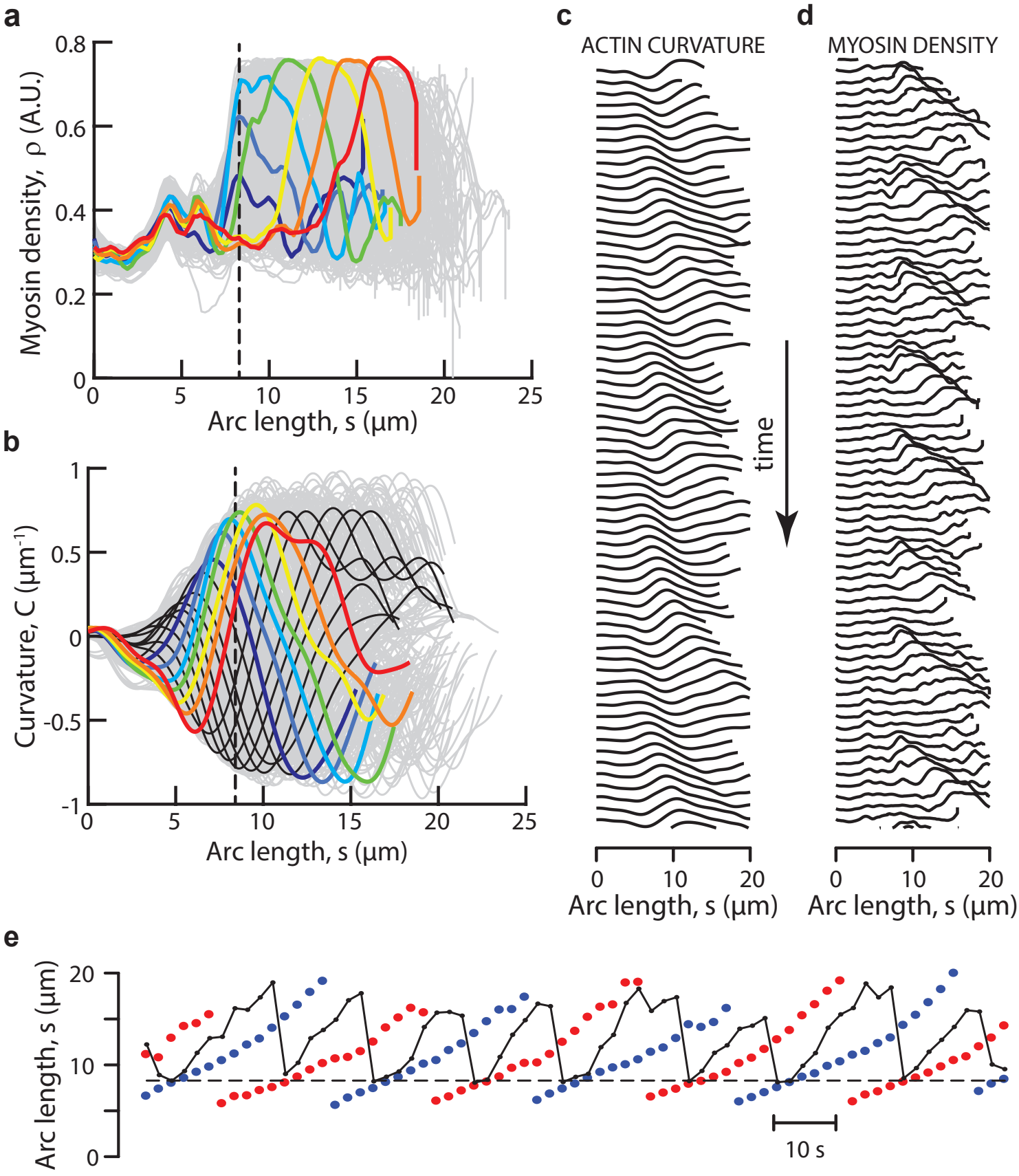
a
Myosin density, ρ (A.U.)
0.8
0.6
0.4
0.2
0
0
5
10
15
20
25
Arc length, s (μm)
b
Curvature, C (μm-1)
1
0.5
0
-0.5
-1
0
5
10
15
20
25
Arc length, s (μm)
c
ACTIN CURVATURE
time
0
10
20
Arc length, s (μm)
d
MYOSIN DENSITY
0
10
20
Arc length, s (μm)
e
Arc length, s (μm)
20
10
0
10 s

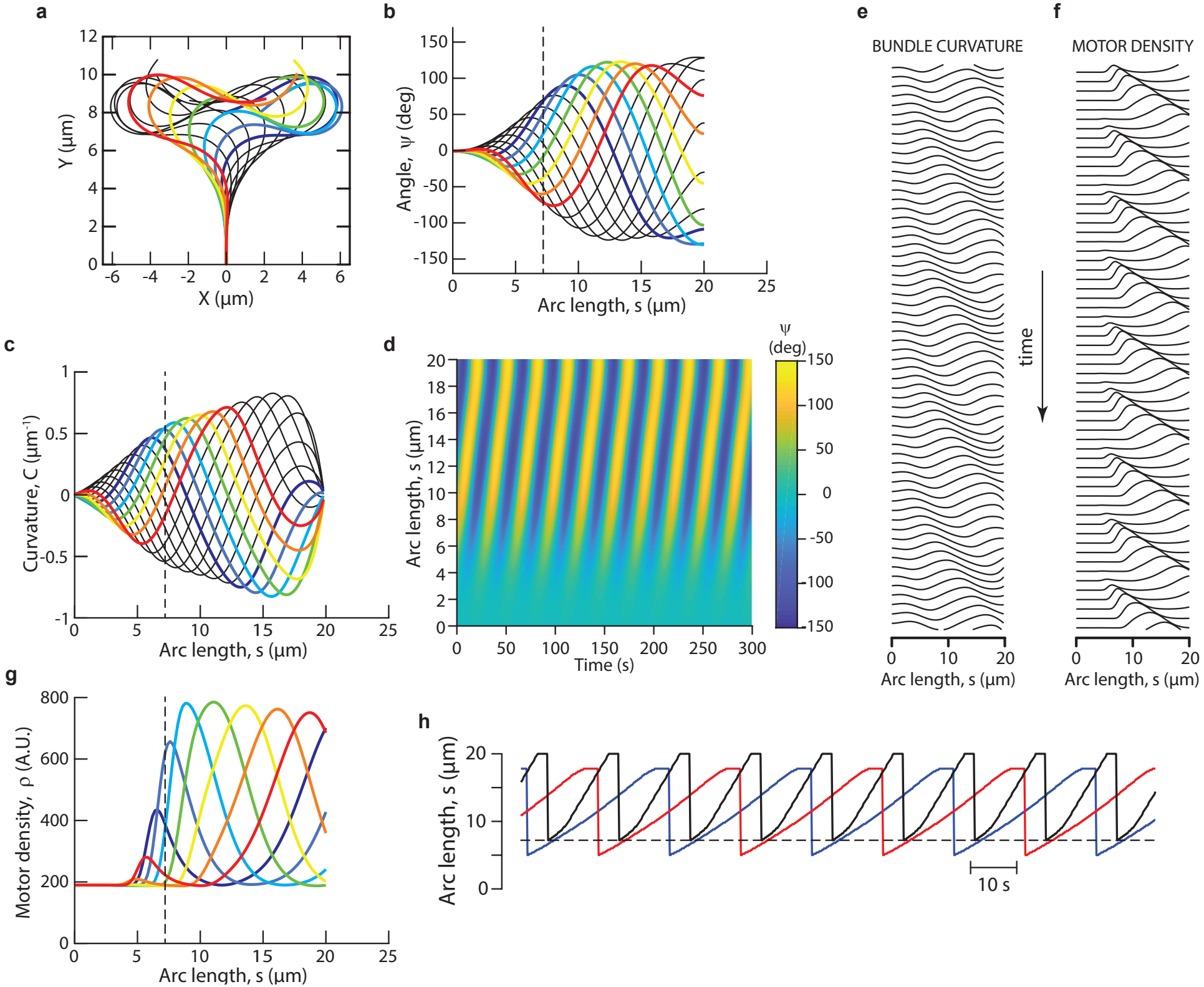
a
Y (μm)
X (μm)
b
Angle, ψ (deg)
Arc length, s (μm)
c
Curvature, C (μm⁻¹)
Arc length, s (μm)
d
Arc length, s (μm)
Time (s)
ψ (deg)
e
BUNDLE CURVATURE
time
Arc length, s (μm)
f
MOTOR DENSITY
Arc length, s (μm)
g
Motor density, ρ (A.U.)
Arc length, s (μm)
h
Arc length, s (μm)
10 s

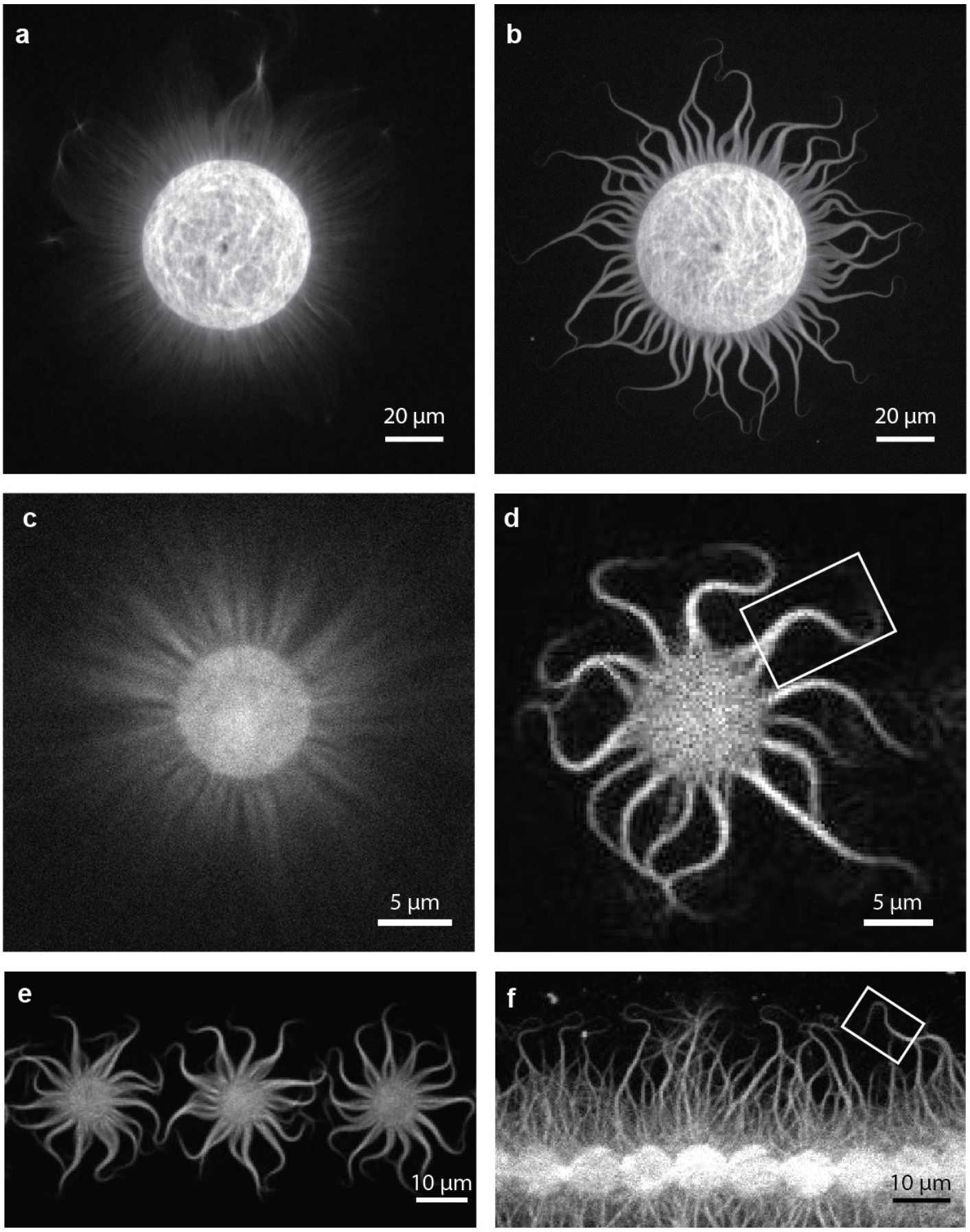
a
20 µm
b
20 µm
c
5 µm
d
5 µm
e
10 µm
f
10 µm

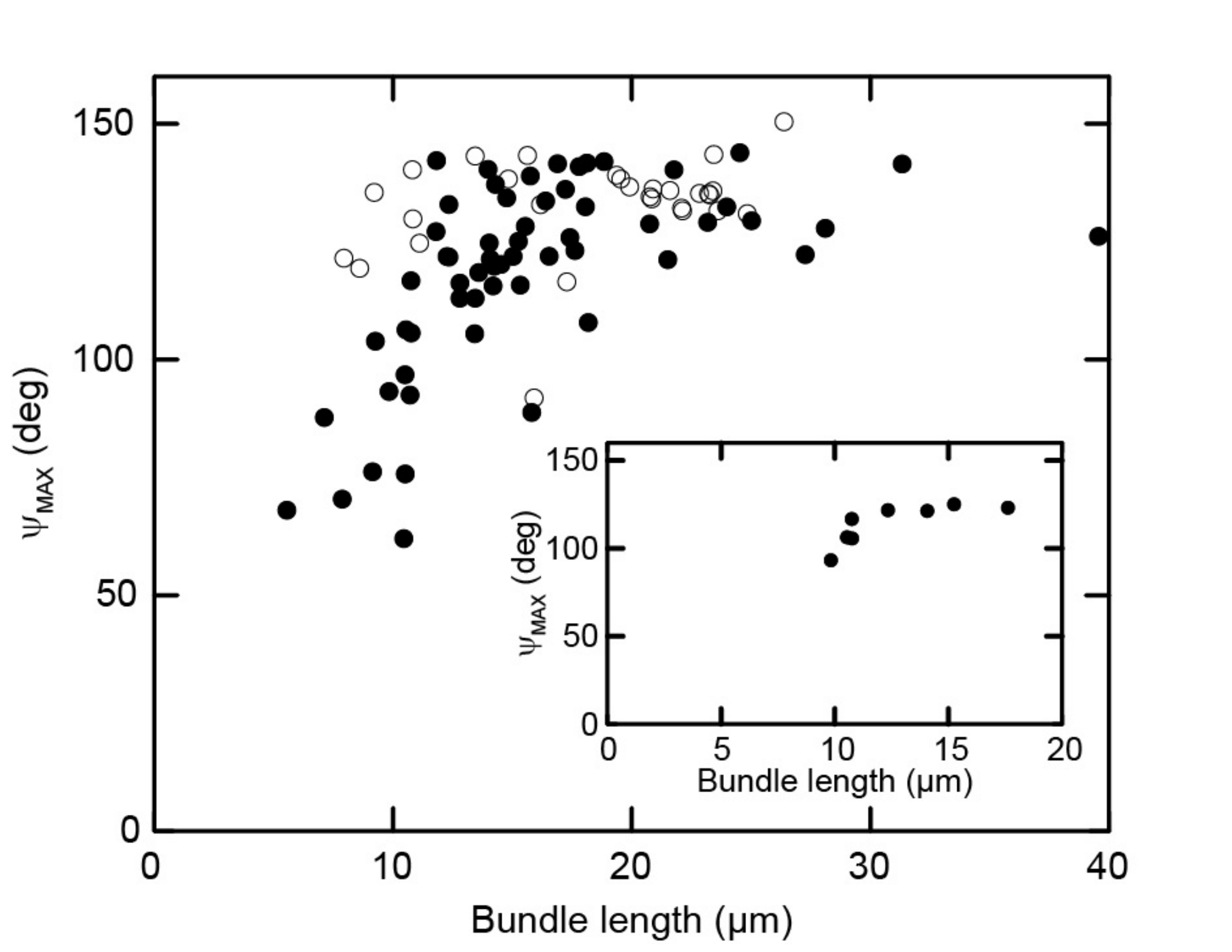
150
100
50
0
0
10
20
30
40
ψ_{MAX} (deg)
Bundle length (μm)
150
100
50
0
0
5
10
15
20
ψ_{MAX} (deg)
Bundle length (μm)

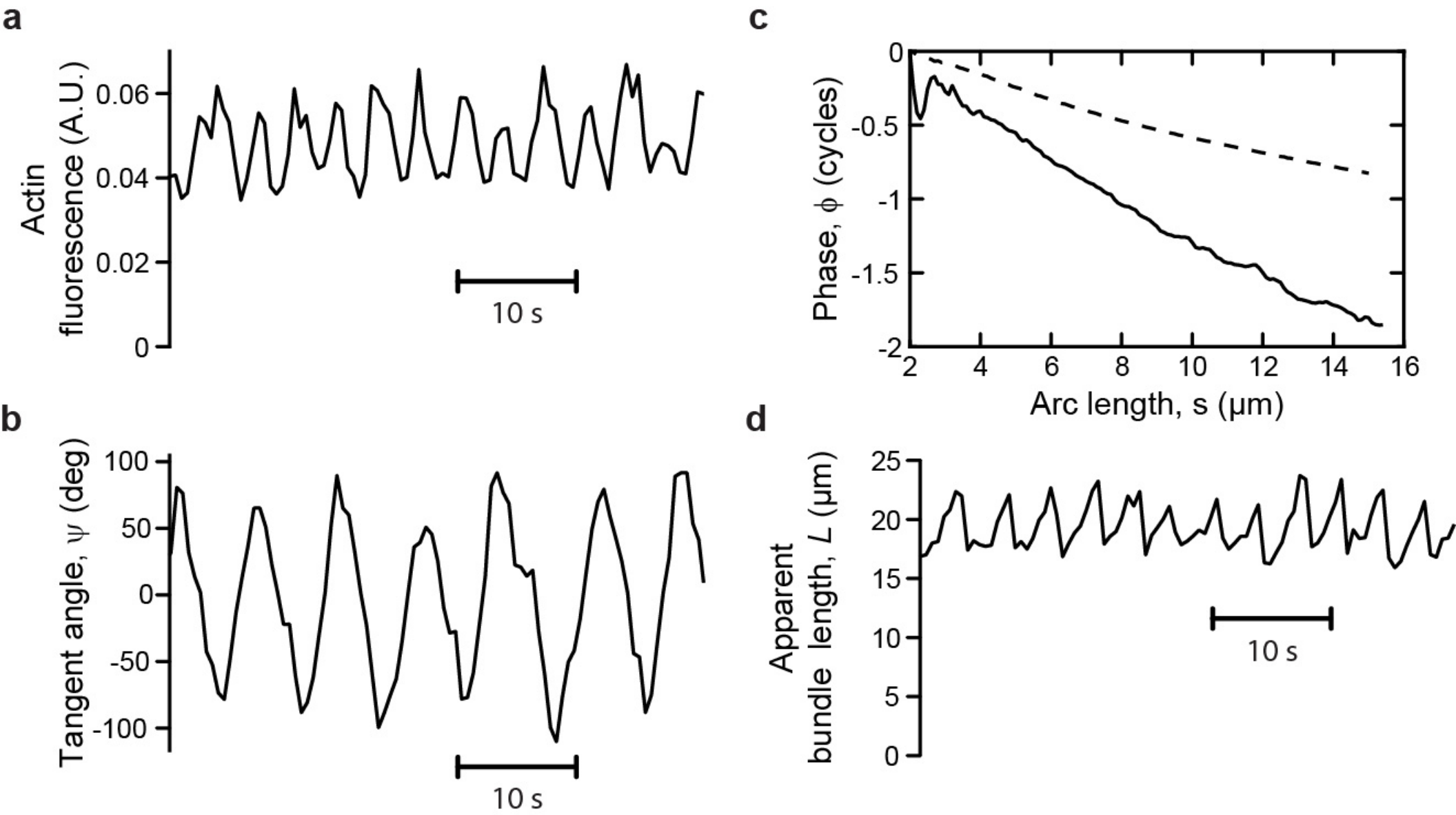
a
Actin fluorescence (A.U.)
0.06
0.04
0.02
0
10 s
b
Tangent angle, ψ (deg)
100
50
0
-50
-100
10 s
c
Phase, ϕ (cycles)
0
-0.5
-1
-1.5
-2
2
4
6
8
10
12
14
16
Arc length, s (μm)
d
Apparent bundle length, L (μm)
25
20
15
10
5
0
10 s

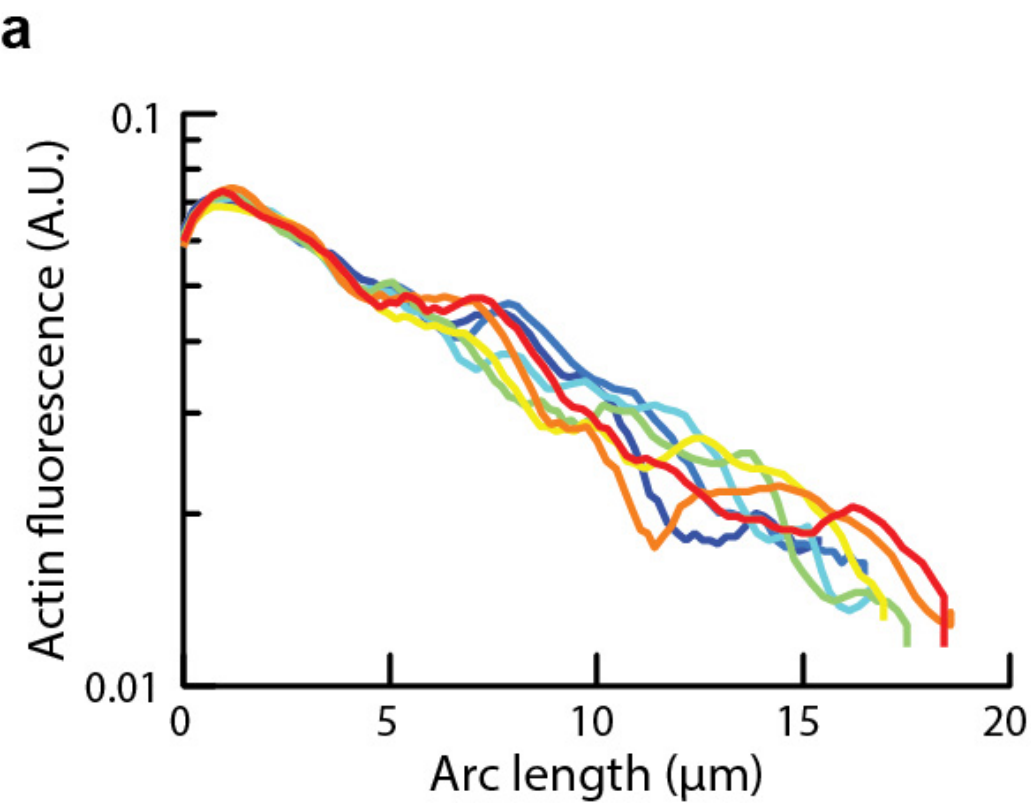
a
0.1
0.01
Actin fluorescence (A.U.)
0
5
10
15
20
Arc length (μm)

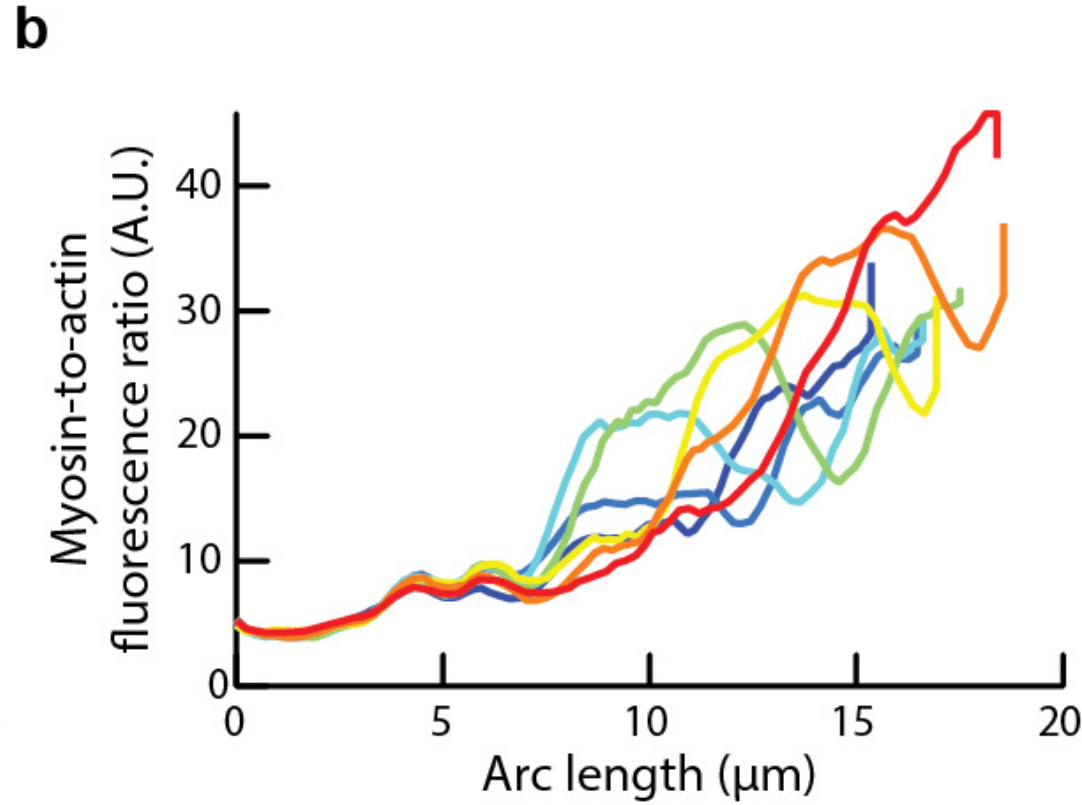
b
40
30
20
10
0
Myosin-to-actin
fluorescence ratio (A.U.)
0
5
10
15
20
Arc length (μm)

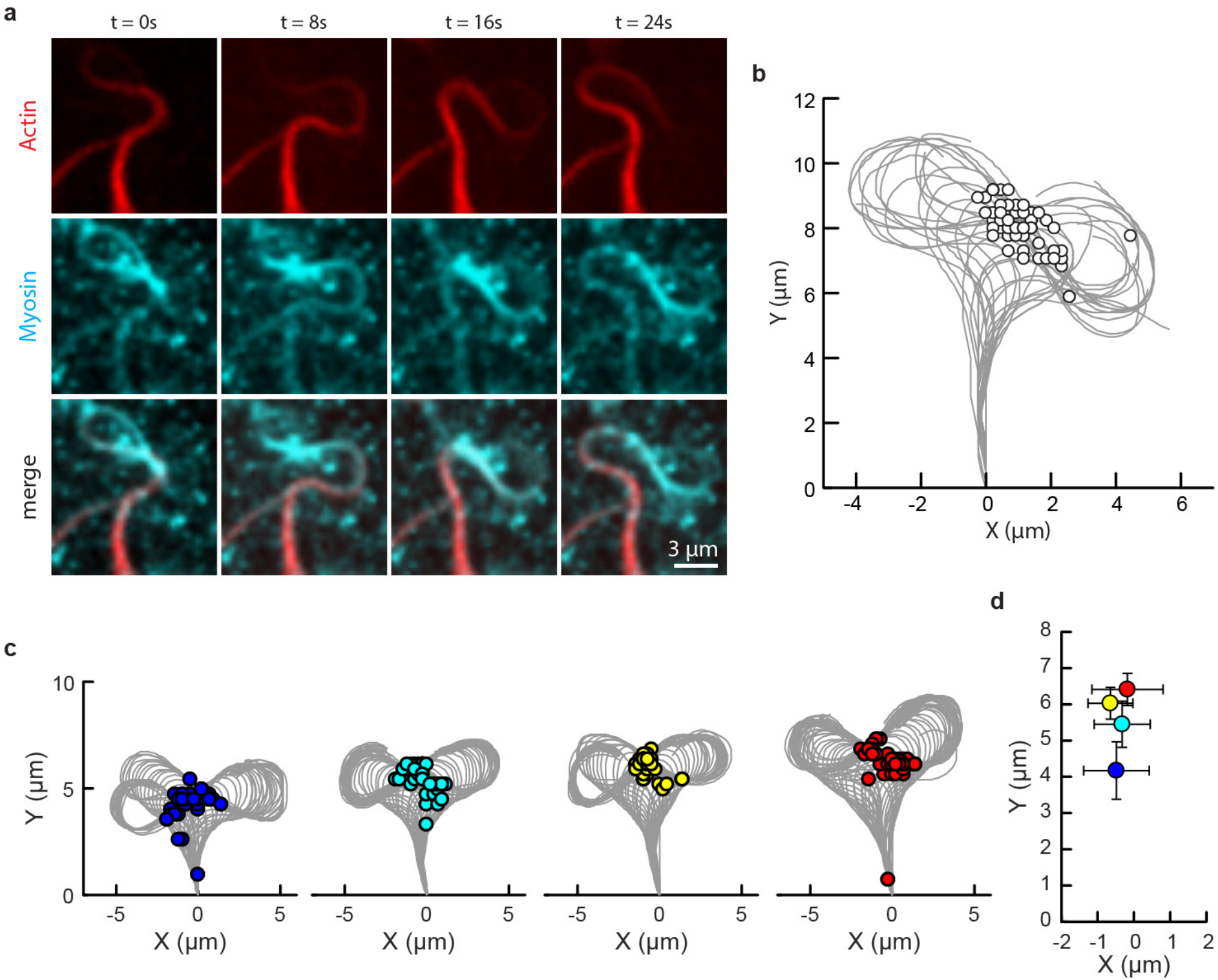
a
t = 0s
t = 8s
t = 16s
t = 24s
Actin
Myosin
merge
3 µm
b
Y (µm)
X (µm)
c
Y (µm)
X (µm)
d
Y (µm)
X (µm)

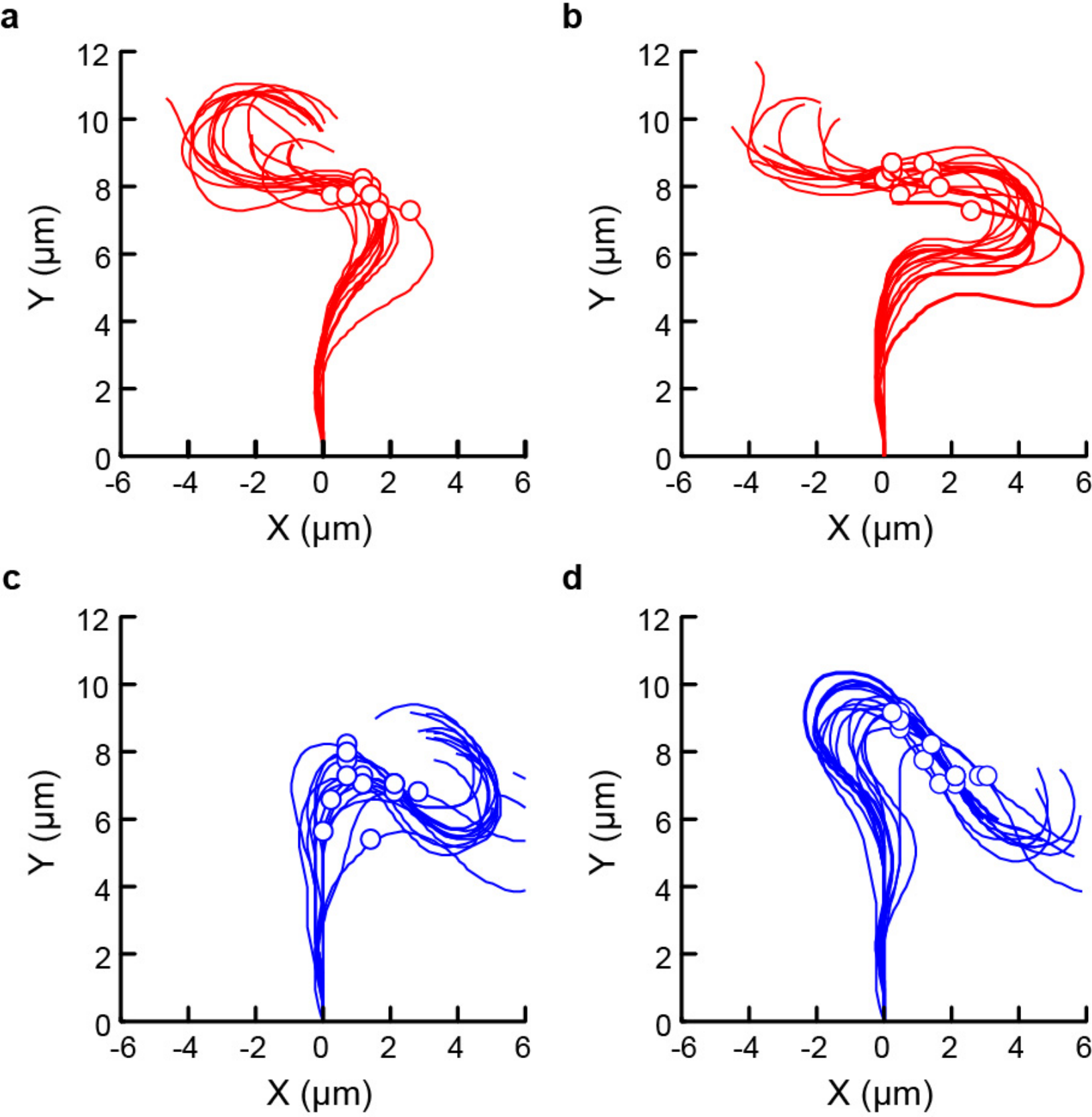
a
b
c
d
Y (μm)
X (μm)
12
10
8
6
4
2
0
-6
-4
-2
0
2
4
6

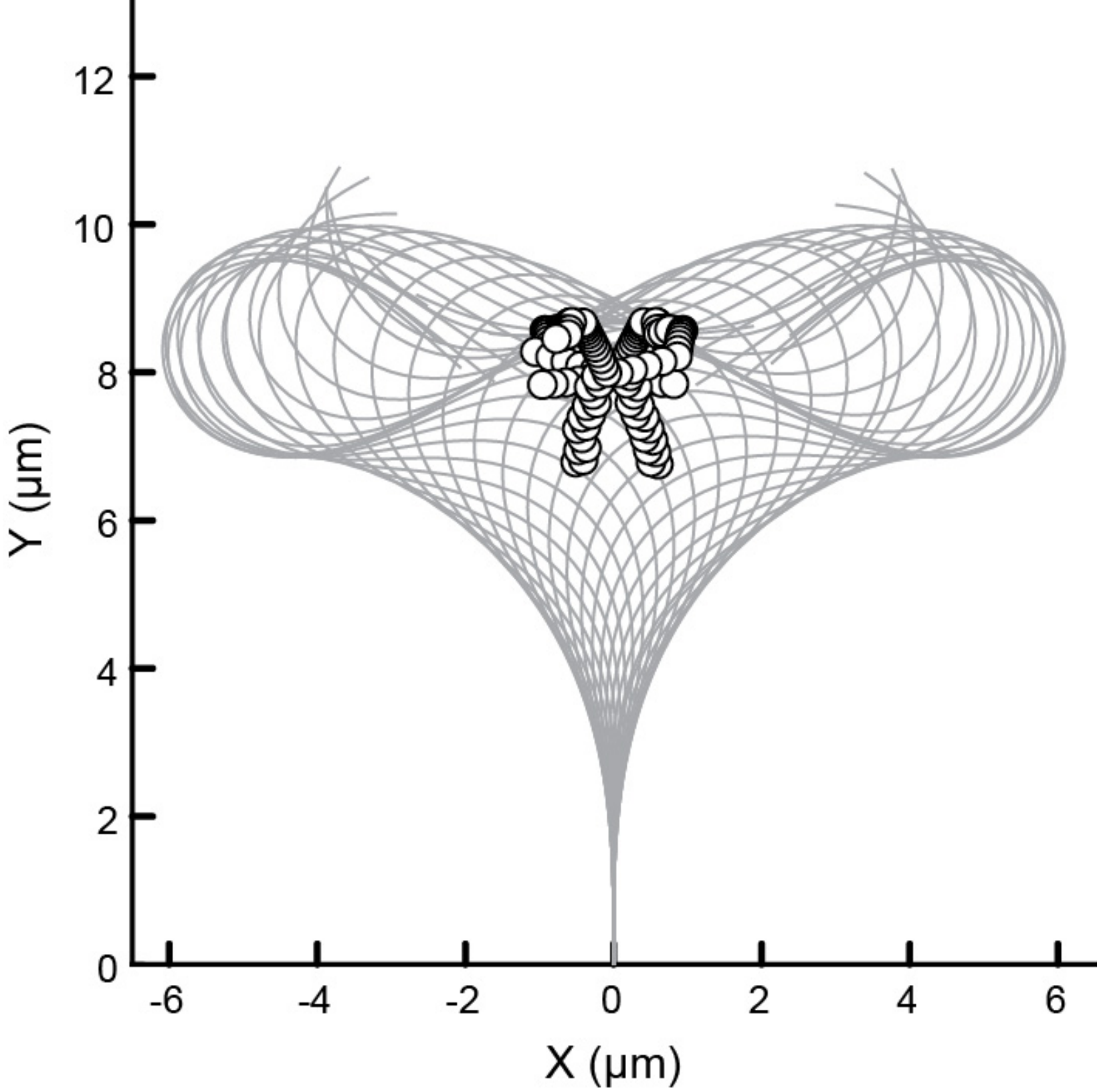
12
10
8
6
4
2
0
Y (µm)
-6
-4
-2
0
2
4
6
X (µm)